

# Self-assembled virus–membrane complexes

LIHUA YANG<sup>1\*</sup>, HONGJUN LIANG<sup>1\*</sup>, THOMAS E. ANGELINI<sup>2</sup>, JOHN BUTLER<sup>1</sup>, ROBERT CORIDAN<sup>2</sup>, JAY X. TANG<sup>5</sup> & GERARD C. L. WONG<sup>1,2,3,4†</sup>

<sup>1</sup>Department of Materials Science and Engineering, <sup>2</sup>Department of Physics, <sup>3</sup>Department of Bioengineering, <sup>4</sup>Frederick Seitz Materials Research Laboratory, University of Illinois at Urbana-Champaign, 1304 West Green St., Urbana, Illinois 61801, USA

<sup>5</sup>Department of Physics, Brown University, Box 1843, 184 Hope St., Providence, Rhode Island 02912, USA

\*These authors contributed equally to this work

†e-mail: gclwong@uiuc.edu

Published online: 15 August 2004; doi:10.1038/nmat1195

**A**nionic polyelectrolytes and cationic lipid membranes can self-assemble into lamellar structures ranging from alternating layers of membranes and polyelectrolytes<sup>1–11</sup> to ‘missing layer’ superlattice structures<sup>12</sup>. We show that these structural differences can be understood in terms of the surface-charge-density mismatch between the polyelectrolyte and membrane components by examining complexes between cationic membranes and highly charged M13 viruses, a system that allowed us to vary the polyelectrolyte diameter independently of the charge density. Such virus–membrane complexes

have pore sizes that are about ten times larger in area than DNA–membrane complexes, and can be used to package and organize large functional molecules; correlated arrays of  $\text{Ru}(\text{bpy})_3^{2+}$  macroionic dyes have been directly observed within the virus–membrane complexes using an electron-density reconstruction. These observations elucidate fundamental design rules for rational control of self-assembled polyelectrolyte–membrane structures, which have applications ranging from non-viral gene therapy<sup>13–16</sup> to biomolecular templates for nanofabrication<sup>17</sup>.

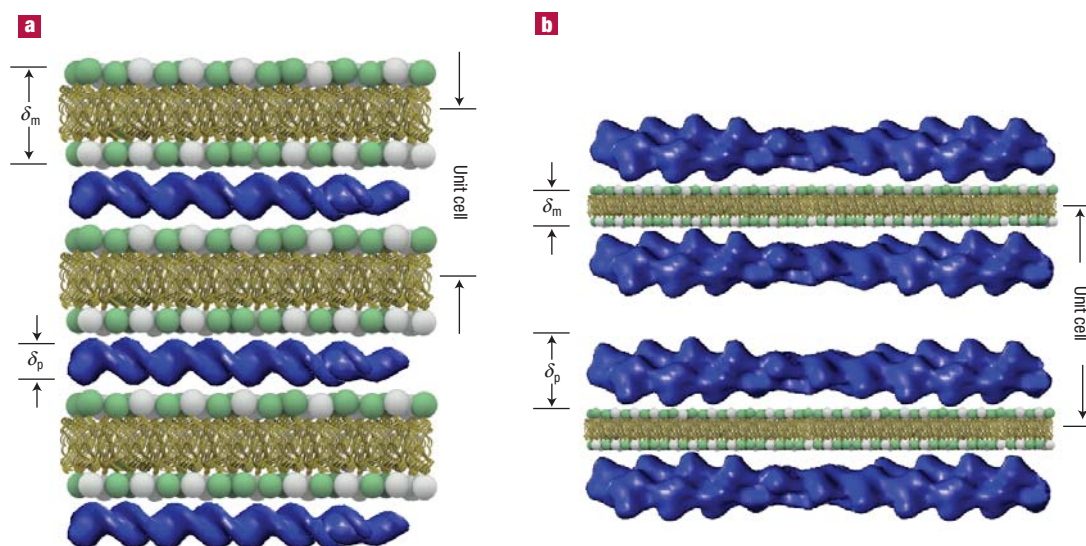


**Figure 1** Representation of polyelectrolyte–membrane complexes. **a**, The DNA–membrane complex has a simple lamellar structure, consisting of alternating polyelectrolyte and membrane layers. **b**, Actin is about four times larger than DNA in diameter. The actin–membrane complex consists of swollen three-layer units. (Note change in relative scale of the two representations.) The representations of F-actin and DNA are low-resolution density maps generated using Situs software (<http://situs.biomachina.org>).

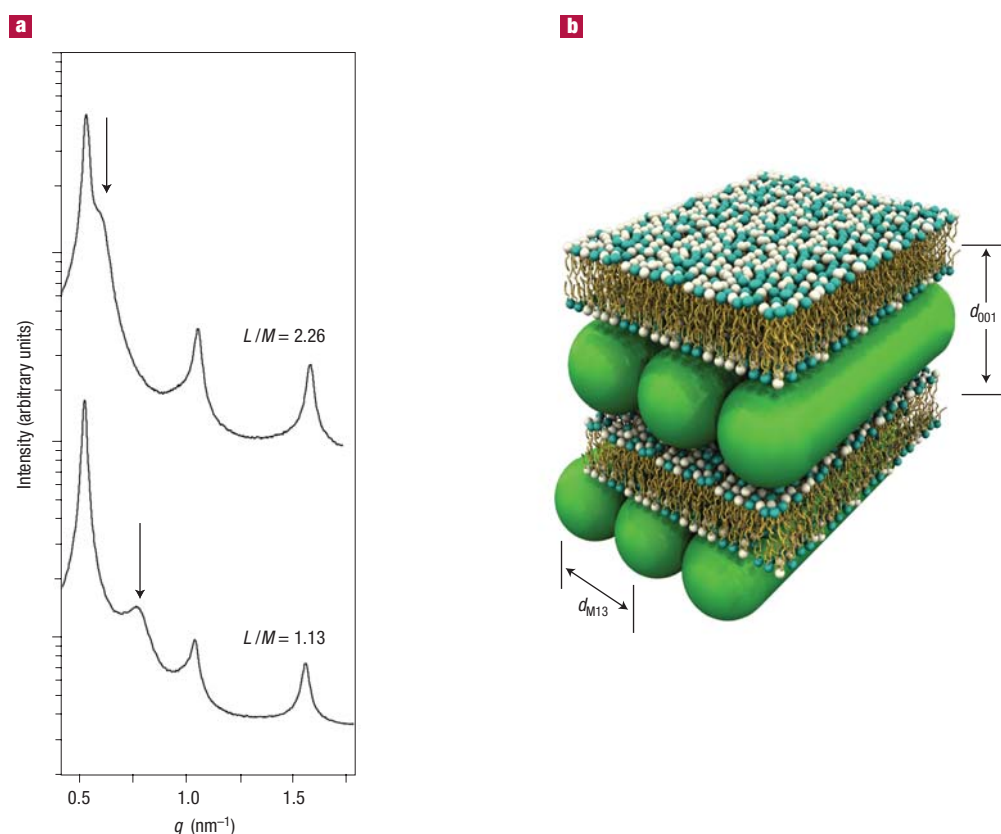


**Figure 2** Complexes between highly charged M13 filamentous viruses and cationic membranes. **a**, Synchrotron SAXS data for charge-density-matched M13–lipid complexes at two different M13–lipid weight ratios,  $L/M = 1.13$ , and  $L/M = 2.26$ . Both cases exhibit equally spaced diffraction peaks expected from a lamellar structure ( $q_{001}$ ,  $q_{002}$ ,  $q_{003}$ ). The peak shift (arrow) in the  $L/M = 2.26$  case indicates an expanded 2D M13 lattice. **b**, The lamellar period of M13–membrane complexes is  $\sim 12.1$  nm, which is enough for the membrane thickness plus a M13 virus diameter. This indicates that the virus–membrane complexes adopt the simple lamellar structure of DNA–membrane complexes, rather than the superlattice structure of actin–membrane complexes.

DNA–cationic membrane complexes organize into a simple lamellar structure, in which a periodic one-dimensional (1D) lattice of parallel DNA chains is confined between stacked 2D lipid sheets (Fig. 1a)<sup>1,5–11</sup>. For such complexes,  $\delta_p < \delta_M$ , where  $\delta_p$  is the polyelectrolyte diameter and  $\delta_M$  is the membrane thickness<sup>1,18</sup>. In actin–cationic membrane complexes, where  $\delta_p > \delta_M$ , the system reconstructs into a ‘missing layer’ superlattice structure, comprising a periodic stack of composite three-layer polyelectrolyte–membrane sheets in which each membrane bilayer is associated with two layers of actin, one on each hydrophilic surface (Fig. 1b)<sup>12</sup>. To investigate the observed polymorphism of lamellar polyelectrolyte–membrane structures, we must be able to independently vary the polyelectrolyte diameter and polyelectrolyte charge density in addition to the membrane charge density, which was done in the pioneering studies. The filamentous bacteriophage M13 virus has a length of  $\sim 880$  nm and a diameter of  $\sim 6.5$  nm (refs 19, 20), which is close to that of F-actin (7.5 nm)<sup>12</sup> and much larger than that of DNA (2.0 nm)<sup>1</sup>. However, M13 has a surface charge density of  $1 e^-/256 \text{ \AA}^2$ , due to its major coat protein, a 50 residue charged  $\alpha$ -helix, which is replicated  $\sim 2,700$  times on the viral surface. This charge density is much higher than that of F-actin ( $1 e^-/625 \text{ \AA}^2$ ), and approaches that of DNA ( $1 e^-/106 \text{ \AA}^2$ ).

Small angle X-ray scattering (SAXS) measurements have been used to monitor the structure of the M13 virus–cationic membrane system, using both an in-house X-ray source as well as a synchrotron source. Because the diameter of the M13 virus is similar to that of F-actin, one

may expect the virus–membrane complexes to assemble into something similar to the superlattice structure of actin–membrane complexes. Representative data for lamellar complexes made using composite membranes of the neutral lipid DOPC (dioleoyl phosphatidylcholine) and cationic lipid DOTAP (dioleoyl trimethylammonium propane) at a DOTAP/DOPC mass ratio of 30/70 is shown in Fig. 2. Two different stoichiometries are shown, denoted by two different  $L/M$  ratios, where  $L$  denotes the weight of lipid (DOTAP and DOPC) whereas  $M$  denotes the weight of M13 viruses. For the virus–membrane complex at  $L/M = 1.13$ , near the isoelectric point, three equally spaced sharp peaks are visible at  $q = 0.52 \text{ nm}^{-1}$ ,  $q = 1.04 \text{ nm}^{-1}$  and  $q = 1.56 \text{ nm}^{-1}$ , which correspond to a 1D lamellar structure with a period of  $d = 2\pi/q_{001} = 12.1$  nm. At a DOTAP/DOPC ratio of 30/70,  $\delta_M$  is estimated<sup>5,21</sup> to be  $\sim 4.3$  nm. The interlayer spacing  $d$  deduced from these three peaks is consistent with  $d = \delta_M + \delta_p$ , the thickness of the membrane plus  $\sim 7.8$  nm, which is slightly larger than one M13 virus diameter ( $\sim 6.5$  nm). The broad peaks (marked by arrows) correspond to the inter-M13 correlation and its position ( $q_{M13}$ ) gives the spacing between M13 viruses confined between lipid membranes. For the sample with  $L/M = 1.13$ , the M13 peak at  $q_{M13} = 0.77 \text{ nm}^{-1}$  gives the corresponding inter-M13 spacing of  $d_{M13} = 2\pi/q_{M13} = 8.2$  nm, which is slightly larger than the diameter of the M13 virus. These results show unambiguously that the virus–membrane complexes adopt the simple lamellar structure of DNA–membrane complexes, rather than the superlattice structure

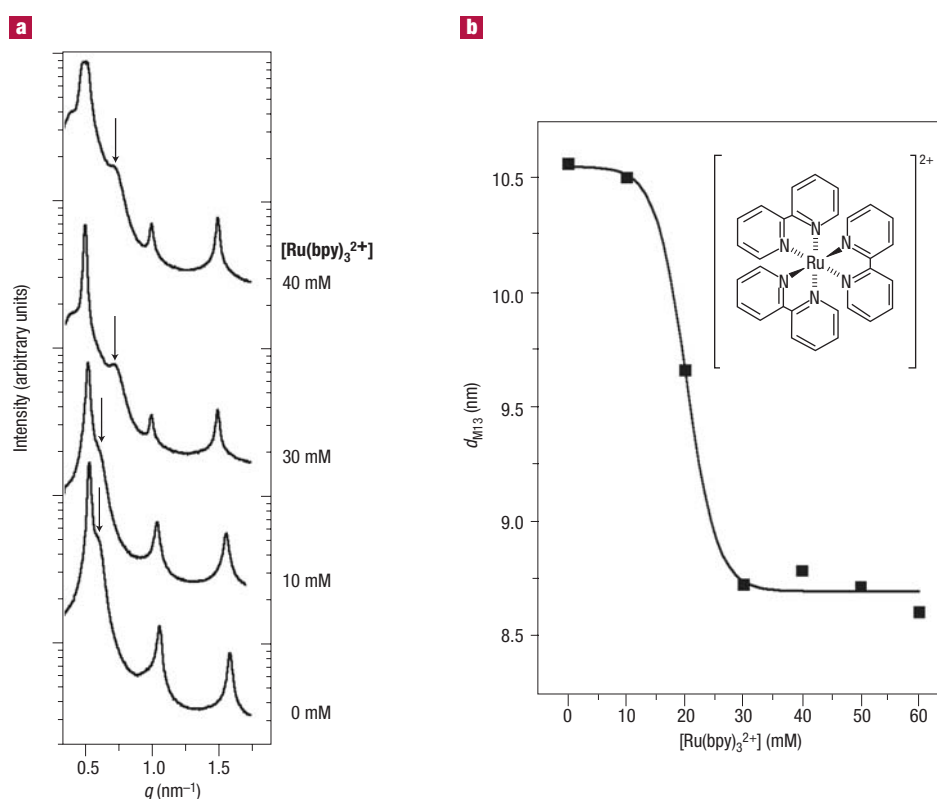


**Figure 3** Organization of nanoscopic arrays of  $\text{Ru}(\text{bpy})_3^{2+}$  macroions by virus–membrane complexes. **a**, The structure of M13–membrane complexes ( $L/M = 2.26$ ) as a function of increasing  $\text{Ru}(\text{bpy})_3^{2+}$  concentration. **b**, The inter-M13 distance as a function of global  $\text{Ru}(\text{bpy})_3^{2+}$  ion concentration: The abrupt decrease of the inter-M13 distance to  $\sim 8.8$  nm at 30 mM signals the co-organization of M13 and dye molecules into a close-packed 2D array. Insert:  $\text{Ru}(\text{bpy})_3^{2+}$ , a large ( $\sim 1.2$  nm diameter) cationic fluorescent dye.

of actin–membrane complexes, consistent with the charge-density-matching mechanism.

The entropic driving force for polyelectrolyte–membrane self-assembly is due to the release of bound counterions as the membrane and polyelectrolyte compensate one another electrostatically<sup>1,5,21,22</sup>. The surface charge densities of DNA and typical cationic lipid membranes ( $1e^-/106 \text{ \AA}^2$  and  $1e^-/70 \text{ \AA}^2$  respectively) are similar, therefore counterion release is maximized for DNA–cationic lipid complexes. By reducing the charge density of the membrane at the charge-neutral DNA–membrane stoichiometry (isoelectric point) by dilution with neutral lipids, the inter-DNA spacing can be continuously adjusted<sup>1,5,21,22</sup> between 2.5 nm (comparable to the hard-core diameter of DNA) and 5.7 nm. F-actin<sup>23</sup>, however, has a much lower surface charge density than that of DNA or typical cationic membranes. Even at maximal neutral lipid dilution (before phase separation), the lowest membrane surface charge density is about  $1e^-/251 \text{ \AA}^2$  (DOTAP/DOPC = 25/75), which is still significantly higher than that for F-actin. Moreover, the F-actin diameter is large (7.5 nm), therefore it is sterically impossible for the F-actin lattice to adjust its lattice spacing to match the membrane charge density. Because the oppositely charged polyelectrolyte and membrane subphases cannot compensate one another's charge, counterion release is impaired. To maximize counterion release and thereby entropy gain, F-actin chains and lipid membranes self-assemble into a ‘missing layer’ superlattice structure, where one layer of membrane is matched against two layers of low charge-density F-actin<sup>12</sup>. A similar structure has been observed in  $\alpha$ -helix-membrane complexes<sup>24</sup>. In contrast, the M13 virus has a

diameter comparable to F-actin but a much higher charge density. For M13–membrane complexes (DOTAP/DOPC = 30/70), close charge-matching between the membrane and the polyelectrolyte is possible, hence the system reconstructs to the simple lamellar structure of DNA–membrane complexes.

It is interesting to note that these virus–membrane complexes can be overcharged<sup>21</sup>. As the lipid–virus stoichiometry is varied from the isoelectric value of  $L/M = 1.13$  to  $L/M = 2.26$ , the inter-M13 spacing increases to  $d_{\text{M13}} = 10.0$  nm (Fig. 2a), which indicates that the lipid-to-M13 ratio within the complex has increased, and that the complexes are positively overcharged. This shows that non-neutral virus–membrane complexes can be stabilized, and such overcharging will impinge on how they interact with cations in aqueous solution and has potential applications for solution templating<sup>25–27</sup> and biomineralization<sup>17,28–30</sup>.

M13 virus–membrane complexes have pore sizes that are  $\sim$ ten times larger in cross-sectional area than DNA–membrane complexes, and may be used to encapsulate and organize large functional molecules, such as proteins, and even protein complexes. Moreover, the M13 virus is a rod-like polyelectrolyte (persistence length  $\xi_p \approx 2 \mu\text{m}$ ), and its bending modulus is  $\sim 40$  times larger than that of DNA ( $\xi_p \approx 50$  nm), so it may be possible to template more ordered structures. For example, although the 2D organization of DNA and point-like ions ( $\text{Mg}^{2+}$ ,  $\text{Ca}^{2+}$ ) within DNA–membrane complexes has been beautifully demonstrated<sup>22</sup>, we have not been able to use DNA–membrane complexes to organize significantly larger molecules.

Figure 3 demonstrates that lamellar virus–membrane complexes can be used to organize nanoscopic arrays of  $\text{Ru}(\text{bpy})_3^{2+}$ , a large

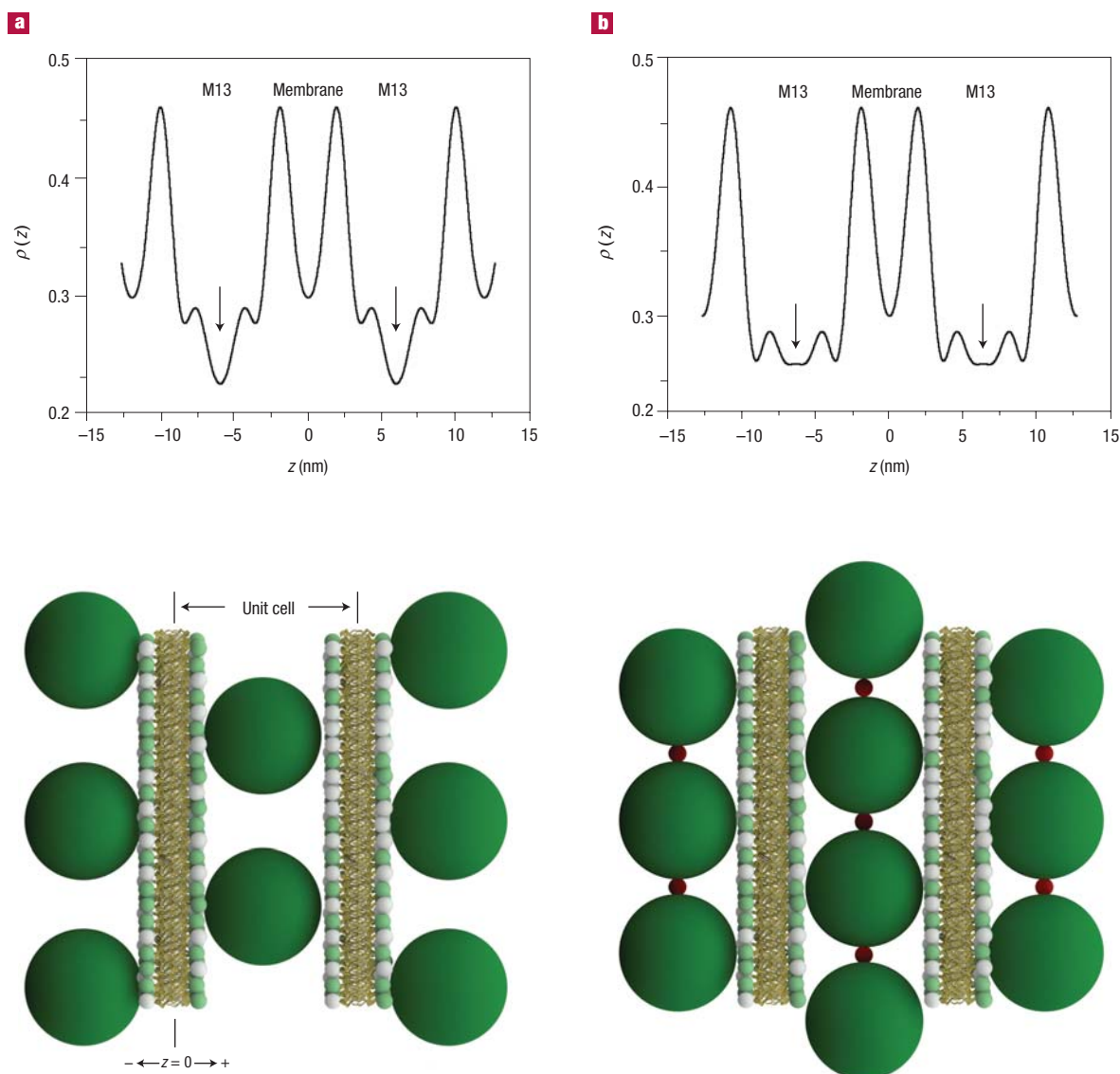


**Figure 4** Electron density  $\rho(z)$  reconstruction of the M13-membrane unit cell. **a, b**,  $\rho(z)$  before (**a**) and after (**b**) the M13 condensation transition at 30 mM  $\text{Ru}(\text{bpy})_3^{2+}$  concentration ( $z$  is defined to be perpendicular to the lipid bilayer.) The highest electron-density peaks coincide with lipid heads, and the low-density regions between two adjacent head groups correspond to their hydrocarbon tails (see the schematics below the reconstruction, roughly aligned with the  $\rho(z)$  reconstruction). Between the membrane sheets is a single layer of M13 viruses. The increase in electron density midway between the membranes (marked by arrows) indicates the position of condensed  $\text{Ru}(\text{bpy})_3^{2+}$  ions (1.2 nm diameter).

(~1.2 nm diameter) cation. The structure of M13-membrane complexes ( $L/M = 2.26$ ) as a function of increasing  $\text{Ru}(\text{bpy})_3^{2+}$  concentration have been measured with synchrotron SAXS (Fig. 3a). The three sharp equally spaced peaks correspond to the first three harmonics of the lamellar structure, and indicate that the overall simple lamellar structure is retained. The broad peaks indicated by arrows corresponds to the inter-M13 correlation. The distance between M13 viruses at various  $\text{Ru}(\text{bpy})_3^{2+}$  concentrations is shown in Fig. 3b. At  $[\text{Ru}(\text{bpy})_3^{2+}] = 10$  mM, the inter-M13 spacing is 10.5 nm, which is essentially the same as that in the complex without  $\text{Ru}(\text{bpy})_3^{2+}$  ions. In this case, the inter-M13 spacing is determined by the membrane surface charge density. As the  $\text{Ru}(\text{bpy})_3^{2+}$  concentration increases to 30 mM, the inter-M13 spacing drops abruptly to ~8.8 nm, which is comparable to the diameter of M13 plus the diameter of  $\text{Ru}(\text{bpy})_3^{2+}$ , and indicates that the  $\text{Ru}(\text{bpy})_3^{2+}$  ions and M13 virus rods have co-condensed

into a 2D close-packed sheet within the simple lamellar M13-membrane complexes, in which the density of  $\text{Ru}(\text{bpy})_3^{2+}$  dye within a lipid gallery is modulated with a spatial period of 8.8 nm by the M13 virus rods. Further increases of  $[\text{Ru}(\text{bpy})_3^{2+}]$  does not significantly alter the inter-M13 spacing.

In order to elucidate the structure of  $\text{Ru}(\text{bpy})_3^{2+}$  within M13-membrane complexes, we have performed electron density  $\rho(z)$  reconstructions of the lamellar unit cell, where  $z$  is along the layering direction. We compared the  $\rho(z)$  profiles of M13-membrane complexes before and after condensation (Fig. 4). The location of the membrane layer can immediately be found by inspection on both structures. The highest electron-density coincides with the phospholipid head groups ( $\sim 0.46 \text{ e} \text{ \AA}^{-3}$ ), and the low-density region between two adjacent head groups corresponds well to that expected from hydrocarbon chains ( $\sim 0.30 \text{ e} \text{ \AA}^{-3}$ ). The distance between the highest

electron-density peaks, 3.8 nm, compares well to the expected thickness of the membrane for DOTAP/DOPC 30/70. Between the membrane sheets, there exists a region ~8.8 nm thick, enough to accommodate one layer of M13 viruses. It is interesting to compare the electron density of this layer before and after condensation (Fig. 4a,b). Water, M13 and Ru(bpy)<sub>3</sub><sup>2+</sup> ions have electron densities of ~0.33 e Å<sup>-3</sup>, ~0.25 e Å<sup>-3</sup> and ~0.41 e Å<sup>-3</sup> respectively. Before Ru(bpy)<sub>3</sub><sup>2+</sup> ions are organized into the lamellar complex ([Ru(bpy)<sub>3</sub><sup>2+</sup>] = 10 mM, Fig. 4a), there is an electron density 'valley' midpoint between two adjacent membranes, where the electron density is mainly contributed by M13, which has a lower electron density than surrounding water and membrane surface. After Ru(bpy)<sub>3</sub><sup>2+</sup> ions are organized into inter-M13 pores ([Ru(bpy)<sub>3</sub><sup>2+</sup>] = 30 mM, Fig. 4b, marked by arrows), this electron density 'valley' has been filled in with extra electron density. This unexpected result indicates that higher electron density Ru(bpy)<sub>3</sub><sup>2+</sup> ions are predominately organized near the tangent contacts between M13 rods. The small bumps on either side are probably due to Fourier truncation effects. A schematic representation that depicts an enhanced density of Ru(bpy)<sub>3</sub><sup>2+</sup> in the midplane of the unit cell is shown in Fig. 4. Structures with small deviations in ion positions from the idealized picture can occur, because the resolution of the reconstruction is ~2 nm. It should be noted that similar phases have been used for both reconstructions. Structural information from this first direct measurement of the condensed ion positions within membrane-polyelectrolyte complexes is important for biomimetic templating, because knowing where the ions are within such complexes is the starting point for rational control.

## METHODS

Freeze-dried M13 and their host *Escherichia coli* (strain K38) were purchased from the American Type Culture Collection (Manassas, Virginia). The progeny phages were separated from the bacteria media by multiple steps of sedimentation and resuspension, followed by a final separation step using the cesium-chloride density gradient method. The M13 virus rods are initially suspended in a pH 7.0 solution (5 mM Tris, 1 mM NaNO<sub>3</sub>). Liposomes comprised of binary mixtures of DOPC and DOTAP are mixed with an aqueous M13 virus solution at controlled stoichiometries to form the self-assembled complexes. All X-ray samples had a final M13 virus concentration of 7.5 mg ml<sup>-1</sup>, and were sealed in quartz capillaries. Ru(bpy)<sub>3</sub><sup>2+</sup> is used in the form of tris(2,2'-bipyridyl)ruthenium(II) (Ru(bpy)<sub>3</sub><sup>2+</sup>) chloride hexahydrate. All polyelectrolyte surface charge densities are estimated using simple cylinder models. The size of Ru(bpy)<sub>3</sub><sup>2+</sup> is estimated using typical values for bond lengths.

SAXS measurements have been used to monitor the structure of M13 virus-membrane complexes, using both an in-house X-ray source as well as the UNICAT beamline 34ID-C at the Advanced Photon Source (APS), Argonne National Laboratory. For the in-house experiments, incident CuK $\alpha$  radiation ( $\lambda = 1.54 \text{ \AA}$ ) from a Rigaku rotating-anode generator is monochromatized and focused using Osmic confocal multilayer optics, and scattered radiation is collected on a Bruker 2D wire detector (pixel size = 105  $\mu\text{m}$ ). For the APS experiment, monochromatic X-rays with energy of 9.93 keV were selected using a Si (111) reflection. Diffraction data were recorded using a Roper Scientific direct-detection CCD (pixel size = 22.5  $\mu\text{m}$ ). The 2D SAXS data from both set-ups have been checked for mutual consistency. Six quasi-Bragg peaks have been used in the  $\rho(z)$  reconstruction, giving a resolution of 2 nm. The procedure for electron density reconstruction is described elsewhere<sup>12</sup>.

Received 29 March 2004; accepted 13 July 2004; published 15 August 2004.

## Reference

1. Radler, J. O., Koltover, I., Salditt, T. & Safinya, C. R. Structure of DNA-cationic liposome complexes: DNA intercalation in multilamellar membranes in distinct interhelical packing regimes. *Science* **275**, 810–814 (1997).
2. Subramanian, G. *et al.* Structure of complexes of cationic lipids and poly(glutamic acid) polypeptides:

A pinched lamellar phase. *J. Am. Chem. Soc.* **122**, 26–34 (2000).

3. Ponomarenko, E. A., Waddon, A. J., Bakeev, K. N., Tirrell, D. A. & MacKnight, W. J. Self-assembled complexes of synthetic polypeptides and oppositely charged low molecular weight surfactants solid-state properties. *Macromolecules* **29**, 4340–4345 (1996).
4. Antonietti, M., Conrad, J. & Thuenemann, A. Polyelectrolyte-surfactant complexes: A new type of solid mesomorphic material. *Macromolecules* **27**, 6007–6011 (1994).
5. Salditt, T., Koltover, I., Radler, J. O. & Safinya, C. R. Two-dimensional smectic ordering of linear DNA chains in self-assembled DNA-cationic liposome mixtures. *Phys. Rev. Lett.* **79**, 2582–2585 (1997).
6. Harries, D., May, S., Gelbart, W. M. & Ben-Shaul, A. Structure, stability, and thermodynamics of lamellar DNA-lipid complexes. *Biophys. J.* **75**, 159–173 (1998).
7. Golubovic, L. & Golubovic, M. Fluctuations of quasi-two-dimensional smectics intercalated between membranes in multilamellar phases of DNA cationic lipid complexes. *Phys. Rev. Lett.* **80**, 4341–4344 (1998).
8. O'Hern, C. S. & Lubensky, T. C. Sliding columnar phase of DNA lipid complexes. *Phys. Rev. Lett.* **80**, 4345–4348 (1998).
9. Bruinsma, R. Electrostatics of DNA-cationic lipid complexes: Isoelectric instability. *Eur. Phys. J. B* **4**, 75–88 (1998).
10. Bruinsma, R. & Mashl, J. Long-range electrostatic interaction in DNA cationic lipid complexes. *Europhys. Lett.* **41**, 165–170 (1998).
11. May, S. & Ben-Shaul, A. DNA-lipid complexes: stability of honeycomb-like and spaghetti-like structures. *Biophys. J.* **73**, 2427–2440 (1997).
12. Wong, G. C. L. *et al.* Hierarchical self-assembly of F-actin and cationic lipid complexes: Stacked three-layer tubule networks. *Science* **288**, 2035–2039 (2000).
13. Felgner, P. L. Nonviral strategies for gene therapy. *Sci. Am.* **276**, 102–106 (1997).
14. Friedmann, T. Overcoming the obstacles to gene therapy. *Sci. Am.* **276**, 96–101 (1997).
15. Lin, A. J. *et al.* Three-dimensional imaging of lipid gene-carriers: Membrane charge density controls universal transfection behavior in lamellar cationic liposome-DNA complexes. *Biophys. J.* **84**, 3307–3316 (2003).
16. Koltover, I., Salditt, T., Radler, J. O. & Safinya, C. R. An inverted hexagonal phase of cationic liposome-DNA complexes related to DNA release and delivery. *Science* **281**, 78–81 (1998).
17. Liang, H., Angelini, T. E., Ho, J., Braun, P. V. & Wong, G. C. L. Molecular imprinting of biomimetic CdS nanostructures: Crystallographic control using self-assembled DNA-membrane templates. *J. Am. Chem. Soc.* **125**, 11786–11787 (2003).
18. Lasic, D. D., Strey, H., Stuart, M. C. A., Podgornik, R. & Frederik, P. M. The structure of DNA-liposome complexes. *J. Am. Chem. Soc.* **119**, 832–833 (1997).
19. Day, L. A., Marzee, C. J., Reisberg, S. A. & Casadevall, A. DNA packing in filamentous bacteriophages. *Annu. Rev. Biophys. Chem.* **17**, 509–539 (1988).
20. Day, L. A., Marzee, C. J., Reisberg, S. A. & Casadevall, A. DNA packing in filamentous bacteriophages. *Ann. Rev. Biophys. Chem.* **17**, 509–539 (1988).
21. Koltover, I., Salditt, T. & Safinya, C. R. Phase diagram, stability, and overcharging of lamellar cationic lipid-DNA self-assembled complexes. *Biophys. J.* **77**, 915–924 (1999).
22. Koltover, I., Wagner, K. & Safinya, C. R. DNA condensation in two dimensions. *Proc. Natl. Acad. Sci. USA* **97**, 14046–14051 (2000).
23. Lodish, H. *et al.* *Molecular Cell Biology* (Scientific American Books, New York, 1995).
24. Koltover, I., Sahu, S. & Davis, N. Genetic engineering of the nanoscale structure in polyelectrolyte-lipid self-assembled systems. *Angew. Chem. Int. Edn* (in the press).
25. Stupp, S. I. & Braun, P. V. Molecular manipulation of microstructures: Biomaterials, ceramics, and semiconductors. *Science* **277**, 1242–1248 (1997).
26. Kresge, C. T., Leonowicz, M. E., Roth, W. J., Vartuli, J. C. & Beck, J. S. Ordered mesoporous molecular sieves synthesized by a liquid-crystal template mechanism. *Nature* **359**, 710–712 (1992).
27. Brinker, C. J. Oriented inorganic films. *Curr. Opin. Colloid Interface Sci.* **3**, 166–173 (1998).
28. Monnier, A. *et al.* Cooperative formation of inorganic-organic interfaces in the synthesis of silicate mesostructures. *Science* **261**, 1299–1303 (1993).
29. Mann, S. *Biomaterialization: Principles and Concepts in Bioinorganic Materials Chemistry* (Oxford Univ. Press, New York, 2002).
30. Hartgerink, J. D., Beniash, E. & Stupp, S. I. Self-assembly and mineralization of peptide-amphiphile nanofibers. *Science* **294**, 1684–1688 (2001).

## Acknowledgements

This material is based upon work supported in part by the US Department of Energy, Division of Materials Sciences under Award No. DEFG02-91ER45439, through the Frederick Seitz Materials Research Laboratory, and carried out in part in the Center for Microanalysis of Materials, which is partially supported by the US Department of Energy under grant DEFG02-91-ER45439, and by NSF-DMR-0409769 and the NSF Nanoscience & Engineering Initiative. Correspondence and requests for materials should be addressed to G.C.L.W.

## Competing financial interests

The authors declare that they have no competing financial interests.